Full length article

Reconstructing dislocation slip evolution by assimilation of elastodynamic displacement signatures

Junjie Yang [a] , Daniel Magagnosc [b] , Jaafar A. El-Awady [a],*, Tamer A. Zaki [a,c],**

[a] *Department of Mechanical Engineering, Johns Hopkins University, Baltimore, MD, 21218, USA*
[b] *DEVCOM Army Research Laboratory, Army Research Directorate, Aberdeen Proving Ground, MD, 21005, USA*
[c] *Department of Applied Mathematics and Statistics, Johns Hopkins University, Baltimore, MD, 21218, USA*

ARTICLE INFO

ABSTRACT

The transient nature of dislocation slip during plastic deformation makes it challenging to track their spatio-temporal evolution from classical measurements. Here, we develop a data assimilation approach to solve the inverse problem of reconstructing the dislocation slip evolution with high spatio-temporal resolution from their elastodynamic displacement signatures. The approach utilizes high-frequency displacement measurements that can be obtained through acoustic-emission sensing or laser interferometry. We employed a total-variation-regularized algorithm to reconstruct the underlying dislocation activities from the acquired displacements. To rigorously assess the capability of the reconstruction algorithm, we acquire the elastodynamic displacement measurements using discrete dislocation elastodynamics simulations as a surrogate for experiment. Our reconstruction quality demonstrates that this approach can accurately capture the underlying evolution of dislocation slip at unprecedented spatio-temporal resolutions beyond conventional defect imaging techniques. The prospective experimental implementation of our reconstruction approach holds promise for providing new understandings into the plastic deformation of advanced materials.

1. Introduction

The plastic deformation of crystalline materials is characterized by intermittent dislocation slip activities [1–4]. Imaging the evolution of these slip activities is crucial for providing new fundamental insights into plasticity mechanisms. However, existing characterization techniques have limitations in visualizing the evolution of dislocation slip. Transmission electron microscopy (TEM) is a powerful tool for imaging dislocations at atomic-level resolutions [5–9], but its applicability is constrained by its transmission imaging principle. TEM can only analyze samples up to a maximum thickness of ∼100 nm, and the behavior of dislocations observed in thin foils may not be representative of those occurring within bulk materials due to the proximity of dislocations to free surfaces. Furthermore, as a direct imaging method, TEM's acquisition time is limited by its charged-couple device camera, which can only achieve a recording rate of around 0.1s [9].

Time-resolved X-ray diffraction techniques at synchrotron facilities are also commonly used to image dislocation slip evolution, but their temporal resolutions, ranging from microseconds to milliseconds, limit their ability to capture transient dislocation movements. X-ray diffraction produces two-dimensional diffraction spots of a three-dimensional

(3D) object, and reconstructing the source 3D object in real time requires a sequence of tilted projections at each frame, prolonging the acquisition time. Several limitations further impact the efficacy of X-ray diffraction techniques for imaging dislocation structures, such as the requirement for samples with low dislocation densities, sensitivity to the crystallographic orientation of the sample, and the need for specialized equipment and instrumentation at synchrotron facilities. Currently, X-ray diffraction topography's applications are confined to isolated nanoparticles (∼0.5 μm in size) [10–13], which may not faithfully represent dislocation behaviors in bulk materials, and the implementation of *in-situ* mechanical loading remains challenging.

To address the limitations of existing characterization techniques, there is a need to develop a new approach that can efficiently and effectively image the evolution of dislocation plasticity. In this work, we introduce a data assimilation approach to reconstruct dislocation slip evolution with high spatio-temporal resolution. Unlike direct imaging methods that rely on capturing photons or particles with a camera, and are thus limited by the camera speed, our approach interprets, or assimilates, high-frequency displacement measurements during the deformation of samples. These measurements can be acquired through acoustic emission (AE) measurements [14] or laser interferometry [15],

---

enabling the resolution of transient dislocation dynamics events. By utilizing the abundance of the information contained in these high-frequency measurements, we solve the data-assimilation inverse problem to reconstruct the underlying dislocation slip evolution. Using the elastodynamic solution of dislocations [16–18], we formulate the data assimilation problem as a linear inverse problem, which has been a subject of extensive research across various disciplines, such as X-ray computed tomography [19,20], restoration of degraded images [21, 22], inference of remote scalar sources from downstream measurements in turbulent environments [23], and applications to nonlinear problems in fluid dynamics [e.g.24–28]. In the following, we introduce a total-variation (TV)-regularized algorithm to reconstruct the underlying dislocation activities from surface measurements and verify the feasibility of our reconstruction approach through discrete dislocation elastodynamics (DDE) simulations.

2. Simulations of dislocation slip evolution and elastodynamic displacement measurements

DDE simulations are conducted to model dislocation slip evolution in face centered cubic (FCC) single crystal Al oriented for single slip. Our simulations are conducted using the open-source code ParaDiS [29] that has been substantially revised in-house [16,30]. In DDE, the elastodynamic displacements induced by dislocation activities, which we intend to detect by high-frequency surface displacement sensors, are modeled using the 3D elastodynamics solution we have previously implemented in ParaDis [16]. It is critical to note that, for the purpose of reconstructing dislocation slip evolution from displacement signals, the latter cannot be approximated by the quasi-static solution of dislocations commonly used in classical discrete dislocation dynamics (DDD) simulations. The identifiability of events happening at different locations and times relies on the dynamic characteristics of waves (e.g., arrival time, amplitude, and wavelength). In classical DDD simulations, the evolution of dislocation networks in FCC metals is less sensitive to the elastodynamic effects under low and intermediate strain rates, or for low/intermediate externally applied stresses [29,31–34]. Therefore, the interactions between dislocations are accounted for using the quasi-static solution [35] as an approximation. All dislocation reactions are planar, and cross-slip mechanisms are not considered in this work for simplicity. The DDE simulation setup is shown in Fig. 1(a). The simulation domain is an Al cube with edges parallel to the $x = [\bar{1}10]$, $y = [\bar{1}\bar{1}2]$, and $z = [111]$ crystallographic directions. The edge length of the simulation cell is 12.8 μm. Free surfaces boundary conditions are imposed on all surfaces. Thirty Frank–Read (FR) dislocation sources are randomly distributed on a plane parallel to the (111) crystallographic plane that is 2.29 nm above the bottom free surface of the simulation cell. Note that the location of the slip plane relative to the bottom surface does not affect the calculations, as there are no elastodynamic displacements calculated on the bottom surface and no dislocations interact with it. All FR sources have a $[\bar{1}10]$ Burgers vector and are generated with random orientations lengths ranging from 1.15 μm to 2.86 μm. A constant shear stress $\sigma_{xz} = 100$ MPa is then applied to the top and bottom surface, such that the $[\bar{1}10](111)$ slip system will have the highest Schmid factor. All dislocations have the same Burgers vector $[\bar{1}10]$. The mechanical properties of Al used in the DDE simulations are listed in Table 1. The simulation time-span is $T = 50$ ns. Unless otherwise specified, twenty-four displacement sensors ($N_s = 24$) evenly surround the plane $z = 6.4$ μm and $z = 12.8$ μm as shown in Fig. 1(a). Although applying multiple sensors to a microscale sample is challenging for AE measurements, it is feasible through surface measurement techniques such as laser interferometry. The data acquisition of these sensors was assumed to be at a time interval $\Delta t_m = 0.1$ ns (10 GHz), over a time horizon $T_m = 57.5$ ns. Note the difference between the simulation time-span T, which is the duration of the deformation process during which dislocations are actively evolving in the DDE simulations, and the measurement

Table 1
Material properties used in the 3D DDE simulations.

Poisson's ratio ν	Shear modulus μ	Burgers vector magnitude b	Density
0.35	26.2 GPa	0.2864 nm	2700 kg/m³

time-span T_m. The measurement time-span extends 7.5 ns beyond the simulation time, totaling 57.5 ns. The additional 7.5 ns ensures that the slowest (transverse) waves can traverse the body diagonal, the longest possible path within the simulation cell. The effect of the acquisition rate is discussed in Section 4.2. The acquisition rate used here is the lowest that still ensures reasonable reconstruction accuracy under the current sensors placement and the strain rate.

The elastodynamic displacement measurements at the 24 sensors are straightforward to calculate by integrating over the surface that has been swept by the dislocations [16]:

$$
\begin{aligned}
\boldsymbol{u}(\boldsymbol{x},t) = &\frac{1}{4\pi} \iint_{S_{cu}|_{t-t'=\frac{r}{c_T}}} \frac{1}{r^3} \left[\frac{12\boldsymbol{r}(\boldsymbol{b}\cdot\boldsymbol{r})(\boldsymbol{n}\cdot\boldsymbol{r})}{r^2} - 3\boldsymbol{b}(\boldsymbol{n}\cdot\boldsymbol{r}) - 3\boldsymbol{n}(\boldsymbol{b}\cdot\boldsymbol{r}) - 2\boldsymbol{r}(\boldsymbol{b}\cdot\boldsymbol{n}) \right] dS'_{cu} \\
&- \frac{1}{4\pi c_T} \frac{\partial}{\partial t} \iint_{S_{cu}|_{t-t'=\frac{r}{c_T}}} \frac{1}{r^2} \left[\boldsymbol{b}(\boldsymbol{r}\cdot\boldsymbol{n}) + \boldsymbol{n}(\boldsymbol{r}\cdot\boldsymbol{b}) - 2\frac{\boldsymbol{r}(\boldsymbol{r}\cdot\boldsymbol{b})(\boldsymbol{r}\cdot\boldsymbol{n})}{r^2} \right] dS'_{cu} \\
&+ \frac{(1-2\nu)}{4\pi(1-\nu)} \iint_{S_{cu}|_{t-t'=\frac{r}{c_L}}} \frac{1}{r^3} \left[\frac{1-3\nu}{1-2\nu}\boldsymbol{r}(\boldsymbol{b}\cdot\boldsymbol{n}) + \boldsymbol{b}(\boldsymbol{r}\cdot\boldsymbol{n}) + \boldsymbol{n}(\boldsymbol{r}\cdot\boldsymbol{b}) - 6\frac{\boldsymbol{r}(\boldsymbol{r}\cdot\boldsymbol{b})(\boldsymbol{r}\cdot\boldsymbol{n})}{r^2} \right] dS'_{cu} \\
&- \frac{(1-2\nu)}{4\pi c_L(1-\nu)} \frac{\partial}{\partial t} \iint_{S_{cu}|_{t-t'=\frac{r}{c_L}}} \frac{1}{r^2} \left[\frac{\nu}{1-2\nu}\boldsymbol{r}(\boldsymbol{b}\cdot\boldsymbol{n}) + \frac{\boldsymbol{r}(\boldsymbol{r}\cdot\boldsymbol{b})(\boldsymbol{r}\cdot\boldsymbol{n})}{r^2} \right] dS'_{cu} \\
&+ \frac{3c_T^2}{2\pi} \int_{1/c_L}^{1/c_T} \iint_{S_{cu}|_{t-t'=\kappa r}} \frac{\kappa}{r^3} \left[\boldsymbol{b}(\boldsymbol{n}\cdot\boldsymbol{r}) + \boldsymbol{r}(\boldsymbol{b}\cdot\boldsymbol{n}) + \boldsymbol{n}(\boldsymbol{b}\cdot\boldsymbol{r}) - \frac{5\boldsymbol{r}(\boldsymbol{b}\cdot\boldsymbol{r})(\boldsymbol{n}\cdot\boldsymbol{r})}{r^2} \right] dS'_{cu} d\kappa
\end{aligned}
$$

(1)

Here, $\boldsymbol{u}$ is the elastodynamic displacement field, $S_{cu}(t)$ is the cumulative surface that has been swept by the dislocation by time t, c_T and c_L are the transverse and longitudinal wave speeds in the isotropic material, ν is the Poisson's ratio, $\boldsymbol{r} = \boldsymbol{x} - \boldsymbol{x}'$ is the vector pointing from the integration point $\boldsymbol{x}'$ to the field point $\boldsymbol{x}$ at which the displacement vector $\boldsymbol{u}$ is to be calculated, r is the magnitude of $\boldsymbol{r}$, and t' is the time when the integration point $\boldsymbol{x}'$ is swept by a dislocation. The surface integral in Eq. (1) represents the integration over all the swept areas for which their associated elastic waves have reached the observer. Fig. 1(b) reports the v_x, v_y, and v_z components of the surface velocity, obtained by taking the numerical derivatives of the displacements measured by a representative sensor marked in red in Fig. 1(a). Notably, The v_x component is stronger than the other two because x is the slip direction. The localization of the displacement signal reflects the heterogeneity of the underlying dislocation plasticity. In the next section, we will discuss the spatio-temporal reconstruction of the slip evolution that decodes the wealth of information contained in these measurements.

3. Reconstructing slip evolution from surface measurements

Dislocations are typically represented by tangled networks, as shown on the slip plane in Fig. 1(a), but in this work, to characterize the slip evolution we generated a—"swept-times map". This map pixelizes the slip plane and counts the number of times each area on the slip plane has been swept, as shown in Fig. 1(c). Unless stated otherwise, a 56×56 mesh is used to discretize the slip plane into pixels measuring $\Delta x = 0.23$ μm each. These pixels are used to record how many times they have been traversed by dislocations every $\Delta t = 0.2$ ns. The swept-times map is a three dimensional tensor that describes the evolution of the footprints of dislocations and, in vectorized form, is denoted s. There are two forms of the swept-times map that we use throughout the paper. The first is the instantaneous swept-times map s_{in}, which records the swept-times of each pixel since the previous time-step and up to the current time-step. The second is the cumulative swept-times map s_{cu}, which records the cumulative swept times of each pixel since
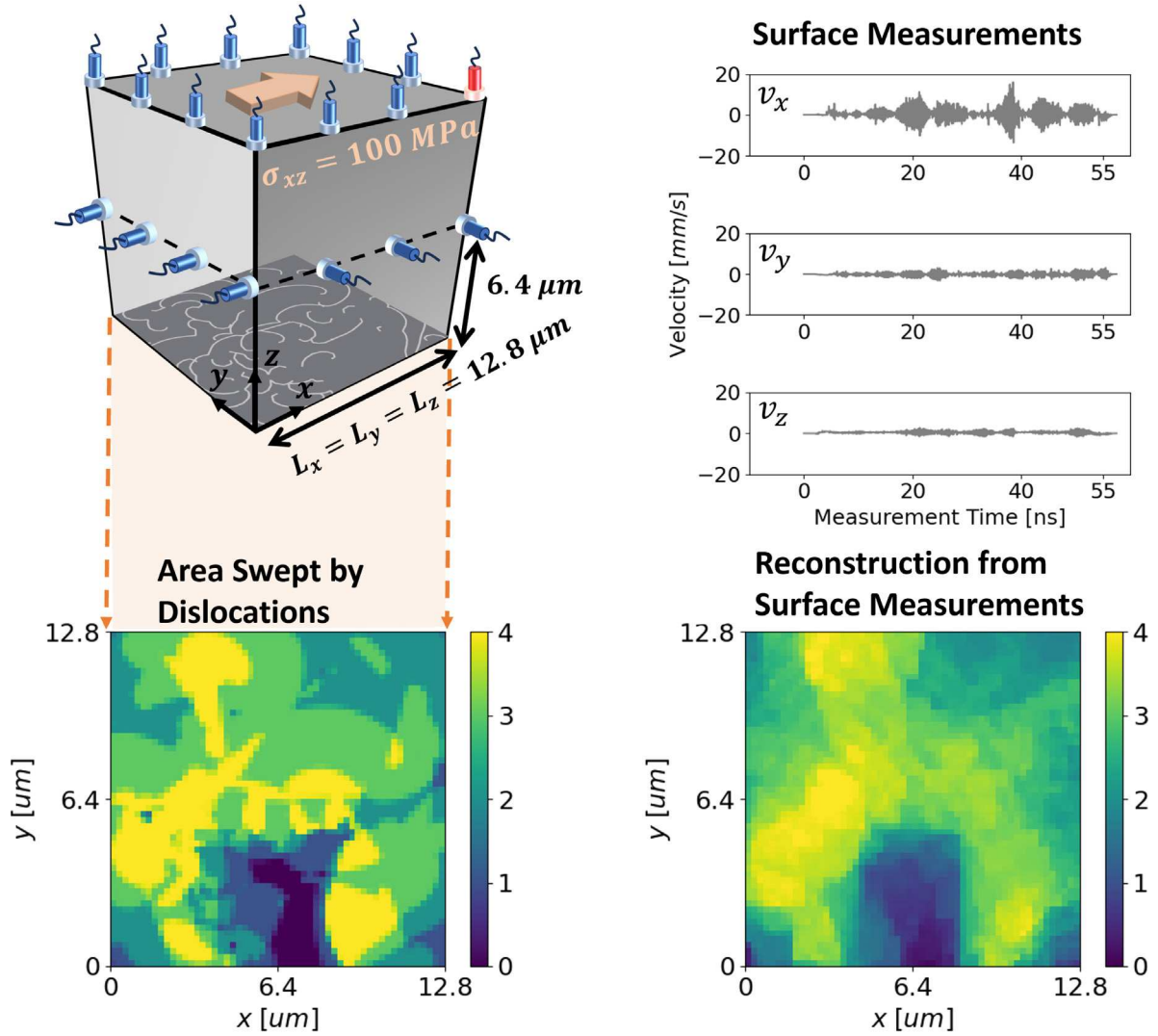
Fig. 1. Schematic showing the reconstruction process of dislocation slip evolution. (a) The DDE simulation configuration. Dislocations are confined to a single slip plane within a free-surface cubic simulation cell. All dislocations are on a plane that is $z = 2.29$ nm above the simulation cell bottom surface. The simulation cell is equipped with 24 high frequency displacement sensors evenly placed on all sides of the simulation cell at two heights $z = 6.4$ μm and $z = 12.8$ μm. (b) The x, y, and z components of the surface velocity obtained by taking the time derivative of the displacements at the sensor marked in red in (a). (c) Cumulative swept-times map on the slip plane at the end of the simulation (t=50 ns). (d) Reconstructed cumulative swept-times map from the surface measurements showing an MSE = 0.34, and SSIM = 0.64. (For interpretation of the references to color in this figure legend, the reader is referred to the web version of this article.)

the initial time and up to the current time. The two maps, s_{cu} and s_{in}, are related as follows:

$$s_{cu} = L_t s_{in}, \qquad (2)$$

where L_t is the integral operator in the time dimension. Due to the invertibility of L_t, the mapping between s_{in} and s_{cu} is one-to-one. It is important to emphasize that they are not two different entities but rather two different representations of the same swept-times map. A positive count is registered for a pixel when a $[\bar{1}10](111)$ dislocation sweeps across the entire area of the pixel by moving in the direction $n \times \xi$, where n and ξ are the slip-plane normal and the line direction of the dislocation, respectively. Conversely, if the dislocation passes through the pixel by moving in the opposite direction, we record a negative count for that pixel. In cases where dislocations only cover a portion of the pixel area, fractional counts are recorded. Fig. 1(c) shows the cumulative swept-times map, and an example in Fig. 2 illustrates the differences and connections between the instantaneous and the cumulative maps.

Swept-times maps are more suitable for characterizing dislocation slip localization as compared to the conventional network representation for two reasons. Firstly, each frame of the swept-times map

provides more information than the dislocation networks. The former not only reflects the current position of dislocation as the contour lines, but also captures the trajectory of dislocations. Furthermore, the swept-times map portrays the localization of plastic deformation, which is difficult to infer directly from a static snapshot of the dislocation microstructure. Secondly, the utilization of the swept-times map naturally arises from the perspective of the elastodynamic solution of dislocations. The elastodynamic field exhibits a complex nonlinear relationship with the evolution of the underlying dislocation network. However, in contrast, the elastodynamic displacement field induced by dislocation motions is linearly related to the swept-time map [16,18], as the swept-times map serves as the integration domain in the surface integral used to calculate the elastodynamic displacement field, as demonstrated in Eq. (1). The linearity significantly simplifies the inverse process of reconstructing slip evolution from elastodynamic field measurements.

As illustrated in Fig. 1, our goal is to reconstruct the swept-times map (Fig. 1(c)) from measurement data (Fig. 1(b)). The swept-times map can be vectorized and denoted s. The dimension of the swept-times map s is $dim(s) = N_t \times N_x \times N_y = 784 \times 10^3$, where $N_t = T/\Delta t = 250$
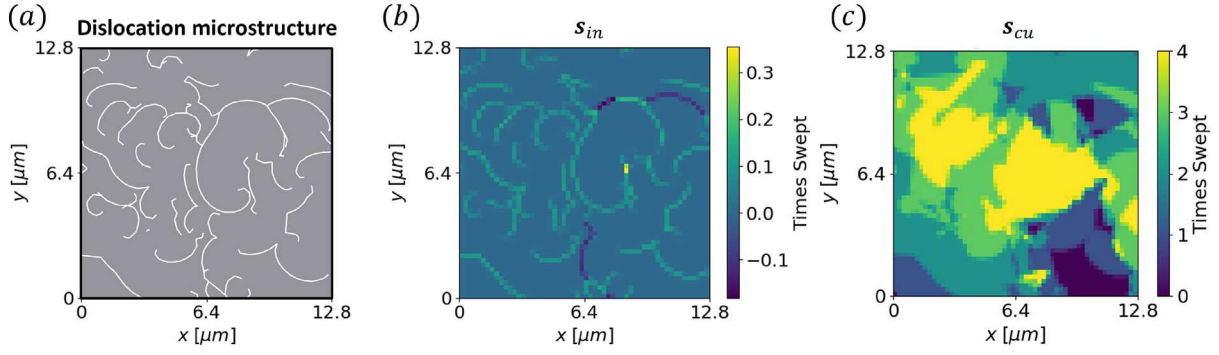
Fig. 2. An example illustrating the two aspects of a swept-times map. (a) Underlying dislocation microstructure that generates the swept-times map in this figure. (b) Instantaneous swept-times map s_{in}, which records the swept-times between the previous and the current time-step. (c) Cumulative swept-times map s_{cu}, which records the cumulative swept times of each pixel from the start to the current state of the dislocation slip evolution.

is the total number of the time-steps, and $N_x = N_y = Lx/\Delta x = 56$ are the numbers of grid points along the x and y directions. The surface velocity at all sensors can be derived from the measured displacements and then aggregated into a single vector $\boldsymbol{v}$. The dimension of $\boldsymbol{v}$ is $dim(\boldsymbol{v}) = 3 \times N_s \times N_{t_m} = 41.4 \times 10^3$, where $N_s = 24$ is the number of sensors, $N_{tm} = T_m/\Delta t_m = 575$ is the number of measurements in time, and the factor of three accounts for each sensor measuring all three components of the displacement. As shown in Eq. (1), the elastodynamic displacement $\boldsymbol{u}$ is a surface integral over the cumulative swept-times map s_{cu}, so they are linearly related: $\boldsymbol{u} \propto s_{cu}$. With the other two obvious linear relationships $\boldsymbol{v} \propto \boldsymbol{u}$ and $s_{cu} \propto s_{in}$, a linear mapping $\boldsymbol{A}$ can be defined between the surface velocity $\boldsymbol{v}$ and the instantaneous swept-times map s_{in}:

$$\boldsymbol{A}s_{in} = \boldsymbol{v}. \tag{3}$$

This linearity originates from the assumption of linear elasticity in the wave medium. The system matrix $\boldsymbol{A}$ has dimensions $dim(\boldsymbol{A}) = (dim(\boldsymbol{v}), dim(s_{in})) = (41.4, 784) \times 10^3$, and is constructed using the elastodynamic solution of dislocations in Eq. (1). Each column of $\boldsymbol{A}$ is the aggregated measurements by the 24 sensors resulting from the activation of a single pixel on the slip plane at one of the time-steps. A noteworthy property of $\boldsymbol{A}$ is its translational invariance in time: the measurements from the activation of a pixel at a later time are simply the translation of measurements from the activation of the same pixel at an earlier time. This property allows for substantial savings in computational memory and time. In practice, only $\frac{1}{N_t}$ of $\boldsymbol{A}$ must be stored, and the remaining portions can be inferred through translations.

Solving for s_{in} given $\boldsymbol{A}$ and $\boldsymbol{v}$ is inherently an ill-posed problem. The system is heavily under-determined, with only $\sim 5\%$ of the total number of measurements compared to the number of unknown variables, not to mention the insufficiency of independent measurements. While the underlying physical processes differ, the mathematical formulation of this reconstruction problem resembles the X-ray computed tomography (CT) reconstruction. In the context of X-ray CT, the source s represents the tomographic image of the object to be reconstructed, the measurement $\boldsymbol{v}$ is the X-ray projections of the object obtained from a series of angles, and the linear mapping relating them is the Radon transform describing how X-rays are attenuated by the object under examination. Given these parallels to X-ray CT reconstructions, we adapt an algorithm that has been widely used in tomographic reconstructions to address the reconstructions of dislocation slip evolution, namely the TV-regularized algorithm [36–38].

We formulate a cost function within the Bayesian inference framework and employ the TV minimization as the regularizer. Specifically, we define the cost as:

$$J(s_{in}) = J_D + J_{L1} + J_{TV}, \tag{4}$$

$$J_D = \frac{\|\boldsymbol{A}s_{in} - \boldsymbol{v}\|_2^2}{2\|\boldsymbol{v}\|_2^2}, \tag{5}$$

$$J_{L1} = \lambda_t \frac{|s_{in}|}{dim(s_{in})}, \tag{6}$$

$$J_{TV} = \frac{\lambda_x |\boldsymbol{D}_x s_{cu}| + \lambda_y |\boldsymbol{D}_y s_{cu}|}{dim(s_{cu})}. \tag{7}$$

Here, J_D, J_{L1} and J_{TV} are the data fidelity term, L1 regularization and TV regularization term, respectively; $\|\cdot\|_2$ is the Euclidean/L2 norm, $|\cdot|$ is the L1 norm, and $\boldsymbol{D}_i$ represents the backward finite difference operator in i direction for every column except the first in i direction; $\boldsymbol{D}_i$ zeros the first column in i direction because the backward operator cannot act on the first step. The coefficients λ's are the weighting factors used to balance the different contributions to the total cost function. A good choice of λ's depends on the characteristics of the swept-times map, which depends on the magnitude of the applied stress and the dislocation density. In practice, the values of λ's are empirically determined from a coarse grid search on another set of DDE simulations with the same applied stress and similar initial dislocation densities as the set to be reconstructed. To empirically determine a reasonable value for λ's without revealing the hidden DDE data to be reconstructed, we conducted an additional set of 50 DDE simulations with the same applied stress and initial dislocation densities as the set to be reconstructed. These 50 DDE simulations served as a testbed for selecting the most effective order of magnitude for λ's. The J_D data fidelity term in Eq. (4) is normalized by the $L2$ norm of the velocity measurement $\|\boldsymbol{v}\|_2$, and the J_{L1} and J_{TV} regularization terms are normalized by the total number of unknowns, $dim(s_{in}) = dim(s_{cu}) = N_t \times N_x \times N_y$. The J_D term in the cost function enforces data fidelity, by penalizing the discrepancies between the reconstructed displacements $\boldsymbol{A}s_{in}$ and the actual measurements $\boldsymbol{v}$. The remaining terms in the cost function are motivated by knowledge of the characteristics of the solution, and attempt to guide the minimization along a favorable path. In particular, J_{L1} promotes sparsity in the instantaneous swept-times map s_{in}. Given that dislocations are sparsely distributed on the plane, this term enforces the regularization that the area swept by dislocations within a time-step Δt should only occupy a small portion of the entire slip plane. Additionally, J_{TV} promotes a piece-wise constant representation of the reconstructed cumulative swept-times map. The underlying rationale is that dislocation movements on the plane should exhibit continuity. The elementary areas swept by the dislocation network at each time frame should seamlessly connect and accumulate in a piece-wise constant maps, with only a few exceptions at junctions or for tiny dislocation segments. This characteristic of the cumulative swept-times map bears similarity to the reconstruction images of X-ray CT, where most objects under examination (e.g. human chest) exhibit piece-wise constant characteristics with clear boundaries. By promoting the sparsity of total variations in the reconstructed images, we effectively remove most abrupt noise pixels that disturb a piece-wise constant representation of the cumulative map, while preserving edges.

With the definition of J in Eq. (4), the reconstruction problem is transformed into the optimization:

$$s_{in} = \arg\min_{s_{in}} J(s_{in}). \tag{8}$$

The gradient of the cost function is:

$$\frac{dJ}{ds_{in}} = \frac{dJ_D}{ds_{in}} + \frac{dJ_{L1}}{ds_{in}} + \frac{dJ_{TV}}{ds_{in}} \tag{9}$$

$$\frac{dJ_D}{ds_{in}} = \frac{A^\top(As_{in} - v)}{\|v\|_2^2} \tag{10}$$

$$\frac{dJ_{L1}}{ds_{in}} = \frac{\lambda_t sign(s_{in})}{dim(s_{in})} \tag{11}$$

$$\frac{dJ_{TV}}{ds_{in}} = \lambda_x \frac{L_t^\top D_x^\top sign(D_x s_{cu})}{dim(s_{in})} + \lambda_y \frac{L_t^\top D_y^\top sign(D_y s_{cu})}{dim(s_{in})} \tag{12}$$

where $D_i^\top$ is the transpose operator of D_i, $L_t^\top$ is the transpose operator of L_t, and $sign(s)$ is an element-wise cut-off sign function:

$$sign(s)_i = \begin{cases} 1, & s_i > \epsilon, \\ -1, & s_i < -\epsilon, \\ 0, & \text{otherwise}. \end{cases} \tag{13}$$

The tolerance $\epsilon = 10^{-6}$ is introduced to prevent excessive computational iterations due to oscillations around zero. The LBFGS algorithm [39,40] is used to minimize the cost function. The optimization terminates when the gradient of the cost function is smaller than 10^{-6}. The most computationally expensive operations in each iteration are the multiplications involving the system matrix A or its transpose $A^\top$, and GPUs are used to accelerate these operations. To alleviate storage cost, the translational invariance of A is exploited. Only $1/N_t$ of A is stored, and the remaining portions are inferred through translations during computations.

The reconstruction process typically requires on the order of one to four hours on a single GPU, depending on the case being considered. The reconstruction of the cumulative swept-times map is presented in Fig. 1(d). In the cost function, $\lambda_t = 10^{-4}$ and $\lambda_x = \lambda_y = 10^{-5}$, which were empirically determined as described above. TV regularization is crucial in mitigating the starvation of information in surface measurements as evidenced by the cost curve in Fig. 3(a). Though TV regularization introduces blocky artifacts and an excessive degree of smoothness in certain regions of the swept-times map as can be seen by comparing Fig. 1(c) and (d), it plays a vital role in preventing overfitting to the measurements and steering the optimization process away from spurious solutions within the infinite solution space. Qualitatively, the reconstruction faithfully captures the location and the approximate shape of the active and inactive plastic regions. However, there are some aspects where the reconstruction is less accurate, for instance, the sharpness of the boundaries across different swept times and the smoothness within the same swept times. In addition, the reconstruction of some regions is slightly shifted compared to the truth. One familiar measure to quantify the fidelity of the prediction is the mean square error (MSE) between the truth and the reconstruction:

$$MSE(x, y) = \frac{1}{N}\sum_{i=1}^{N}(x_i - y_i)^2, \tag{14}$$

where N is the total number of pixels in the image. However, MSE can be inadequate for evaluating perceived image quality because it is calculated pixel-wise and does not consider structural information beyond the pixel of interest [41]. For this reason, we use the structural similarity index (SSIM) [42] to evaluate the reconstruction quality. SSIM is defined as the product of three terms:

$$SSIM(x, y) = \left(\frac{2\mu_x\mu_y + C_1}{\mu_x^2 + \mu_y^2 + C_1}\right)\left(\frac{2\sigma_x\sigma_y + C_1}{\sigma_x^2 + \sigma_y^2 + C_1}\right)\left(\frac{\sigma_{xy} + C_3}{\sigma_x\sigma_y + C_3}\right), \tag{15}$$

where μ_x, μ_y, σ_x, σ_y and σ_{xy} are the local means, standard deviations and the cross correlation for swept-times maps x and y. In the language of image processing, these three terms evaluate the similarity of the two maps in luminance, contrast, and structure. These statistics are calculated locally within a sliding Gaussian weighting window that moves pixel-by-pixel across the image, resulting in an SSIM map. The standard deviation of the Gaussian window is chosen to be 4.5 pixel length which is $\sim 10\%$ of the image length. SSIM values range from -1 to 1. A value closer to 1 indicates better reconstruction quality. The SSIM score of the entire image is the arithmetic average of the SSIM map. The constants C_1, C_2 and C_3 are small positive values that prevent the singularity of each term, and the default values are used from the built-in MATLAB function $ssim$. The SSIM we report hereafter always refer to cumulative swept-times map unless otherwise stated.

To assess the reconstruction quality not only at the final state but throughout the entire dynamic process of dislocation slip, Fig. 3(b) presents the SSIM score for the *in-situ* reconstructions of the instantaneous and cumulative swept-times maps, throughout the loading time. The low-quality and variability of the former suggest that the available measurements do not allow precise reconstruction of the exact occurrence time of dislocation activities. However, the reconstruction of the cumulative swept-times map, which has lower requirements on the temporal accuracy, improves in quality during the later stage. The lower accuracy in the early stage of deformation is attributed to the lack of temporal resolution in the measurements and can potentially be improved by increasing the acquisition rate, as will be discussed in later sections. Indeed, considering the severely ill-posed nature of this inverse problem, the quality of the reconstructions achieved thus far is quite remarkable.

The local similarities between the hidden true swept-times map in Fig. 1(c) and its reconstruction in Fig. 1(d) are assessed in the SSIM map shown in Fig. 3(c). The SSIM score for the reconstruction at the last loading time-step is 0.64. As seen in the comparison between Figs. 1(c) and (d), this level of similarity is sufficient to localize major plastic deformation and to identify its intensity, which supports the use of our algorithm as a potential non-destructive imaging and evaluation technique for crystal plasticity. Overall, the present results demonstrate the potential of the proposed approach to reconstruct dislocation slip evolution with high spatio-temporal resolution, and to offer valuable insights into crystal plasticity.

4. Discussion

4.1. The effect of the number of sensors

In this section, we discuss the influence of the number of sensors on the reconstruction accuracy. Four different cases are considered, $N_s = \{24, 16, 8, 4\}$. In order to statistically examine the reconstruction accuracy, fifty DDE simulations are randomly initialized. In this case, the cubic simulation cell is shown in Fig. 4(a), and it has an edge length of 4.6 µm. Free surfaces boundary conditions are imposed. Twenty $[\bar{1}10](111)$ Frank-Read (FR) sources are randomly distributed on the slip plane that is 2.29 nm above the bottom surfaces of the simulation cell, with randomly generated orientations and lengths ranging from 0.86 µm to 1.72 µm. A constant shear stress $\sigma_{xz} = 50$ MPa is then applied to activate the slip system. The simulation duration is $T = 50$ ns. Sensors are positioned at two different planes parallel to the dislocations slip plane at heights: $z = 2.3$ µm and $z = 4.6$ µm, as shown in Fig. 4(b)–(e). These sensors operate at an acquisition rate of 1 GHz (an order of magnitude lower than the example in Section 2), and the measurements spans a duration of $T_m = 55$ ns, which is sufficiently long for all displacement waves from the final simulation time-step to reach the farthest sensor. The reconstruction algorithm does not rely on specific assumptions about the relative position between the slip plane and the sensor plane. If sensor placement changes from parallel planes to inclined planes, the reconstruction process remains the same except that the system matrix A needs to be re-evaluated for the inclined sensor plane. A 20×20 mesh with the same resolution $\Delta x = 0.23$ µm as discussed in Section 3 is used to record the swept-times. For these
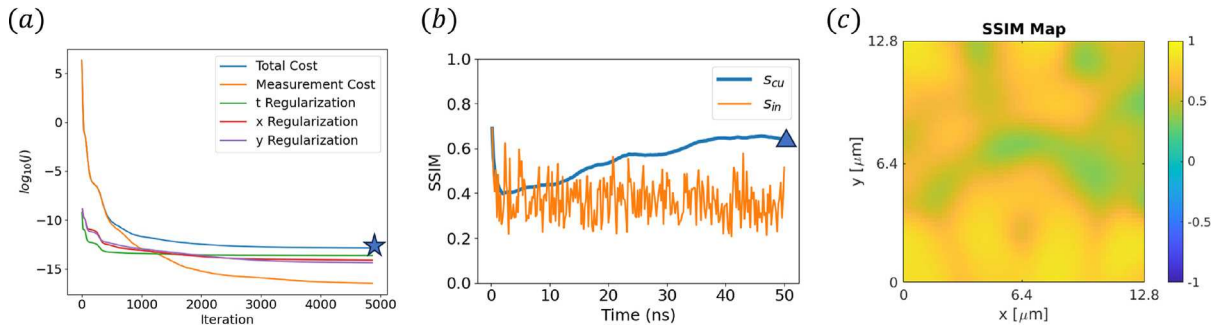
Fig. 3. (a) The convergence curve of each term in the cost function described in Eq. (4). (b) Frame-by-frame reconstruction SSIM computed for both the cumulative and the instantaneous swept-times maps over the loading time at the convergence indicated by the star in (a). (c) The SSIM map between the cumulative swept-times map in Fig. 1(c) and its reconstruction in Fig. 1(d) at the final evolution state indicated by the triangle in (b). The SSIM at each pixel is computed locally using a Gaussian function with standard deviation of 4.5 pixel length to weight the neighborhood around the pixel for estimating the local statistics.
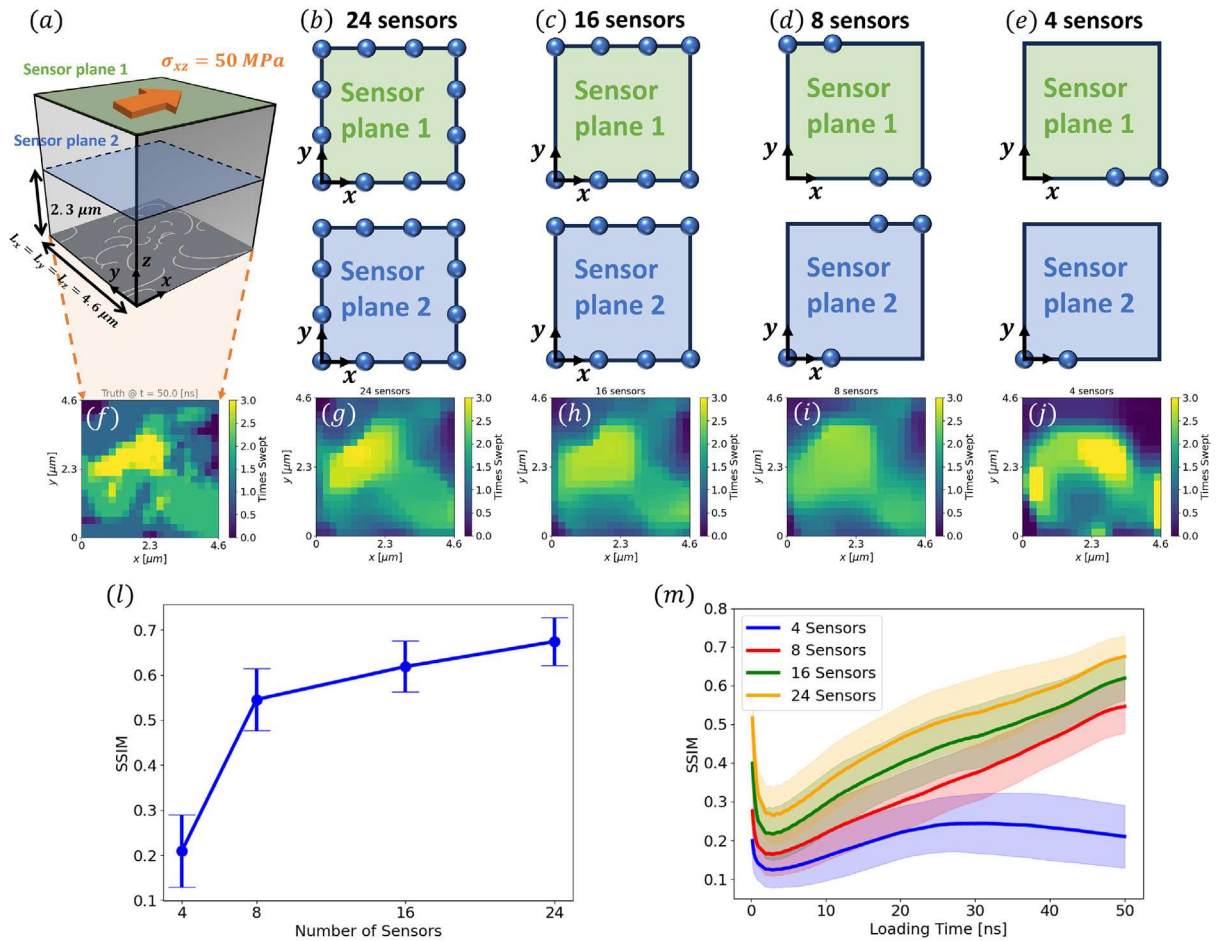

Fig. 4. Effect of the number of sensors on the reconstructions accuracy. (a) Schematic illustration of the configuration of DDE simulations and the position of the two sensor planes used in the study. (b)–(e) Sensor placements on the two planes for 24, 16, 8, and 4 sensors, respectively. (f) A representative cumulative swept-times map at the end of the simulation, whose reconstructions from varying number of sensors are shown in (g)–(j). The SSIM scores for each reconstruction is 0.64, 0.59, 0.55 and 0.29, respectively. (l) Statistical plot of the SSIM for the cumulative swept-times map over 50 randomly initialized DDE simulations for each number of sensors. The dots represent the mean SSIM, and the error bars indicate the standard deviation. (m) Statistical plot for the frame-by-frame reconstruction SSIM of the cumulative swept-times map versus the simulation time. The curves are the mean SSIM at each time-step, and the bands indicate the standard deviation.

reconstructions, the weights in the cost function were $\lambda_t = 10^{-3}$ and $\lambda_x = \lambda_y = 10^{-6}$. All other simulation parameters remain the same as those discussed in Section 3 unless noted.

Fig. 4(f) illustrates the swept-times map for one of the fifty cases, while Figs. 4(g)–(j) showcase the corresponding reconstructions with different number of sensors. As the number of sensors is decreased, the available information becomes progressively less to accurately assess the slip intensity, resulting in blurry edges. Nevertheless, the approximate localization of slip events is still discernible, as observed in the cases with 16 and 8 sensors. However, when only 4 sensors are employed, the potential solution space expands to such an extent that it becomes nearly impossible to confidently infer any features of the dislocation slip evolution from the measurements. As a result, the reconstructions become highly erroneous as observed in Fig. 4(j).

The average SSIM and its standard deviation over the fifty test cases are reported in Fig. 4(l), which reveals that employing a greater number of sensors enhances the average reconstruction quality (the mean of SSIM) while also diminishing the uncertainty (the standard deviation of SSIM) in the reconstruction. This improvement is attributed to the extra independent information provided by the additional sensors that assist in capturing the elastodynamic signatures. Fig. 4(m) shows the statistical reconstruction SSIM as a function of the loading time. This figure demonstrates that increasing the number of sensors improves the reconstruction accuracy across the entire loading time. Consistent with earlier results in Section 3, later processes are reconstructed more accurately than earlier ones. The inaccuracy in reconstructing the earlier stages can be improved not only by increasing the number of sensors, but also by increasing the sensor acquisition rate as we will discuss in the following section.

4.2. Acquisition rate of sensors

In this analysis, we examine the impact of the sensors acquisition rate on the reconstruction accuracy of slip evolution in the same fifty DDE simulations described in Section 4.1. Specifically, eight sensors are used, and their locations are schematically indicated in Fig. 5(a). We compare the reconstruction of the slip evolution when the acquisition rates of the sensors are 10, 5, and 1 GHz. In all the reconstruction tests, the coefficients for the terms in the cost function are $\lambda_t = 10^{-3}$ and $\lambda_x = \lambda_y = 10^{-6}$.

For one of the fifty DDE simulations, we showcase the true cumulative swept-times map at the end of the loading process in Fig. 5(b). In this map, the dislocation activities are localized at the top-right corner, while the lower-left corner remains slip-free. The resulting surface velocities derived from the displacements measured by one of the sensors at different rates are displayed in Fig. 5(c)–(e). The differences in measurement acquisition rates reflect the density of information contained in the signals. It is worth noting that the difference in the magnitude of the surface velocity in the sensor signals is because the sensors register the average velocity between two acquisitions, instead of the instantaneous values.

The reconstructed cumulative swept-times maps are presented in Fig. 5(f)–(h). Both visual observation and SSIM scores clearly demonstrate that higher-frequency sensor signals yield reconstructions with finer details. Despite the scarcity of information in the 1 GHz measurements, it is noteworthy that the positions and intensities of dislocation slip are still accurately reconstructed. This level of accuracy is not possible if not for the design of the cost function, which seeks to identify contiguous regions of cumulative swept-times maps, using the TV regularization. Without these terms in the cost function, the predictions at the low acquisition rate are otherwise very poor.

We also verified that the improvement in reconstruction accuracy with increased acquisition rate persists in a statistical sense. Fig. 5(i) reports the reconstruction SSIM score of the cumulative swept-times map at the final state as a function of the sensor sampling rate. Both the average score and the standard deviation over the fifty cases are

reported. Increasing the acquisition rate by an order of magnitude leads to an increase in the average SSIM score from 0.54 to 0.64. We also report statistical results for *in-situ* reconstructions of the cumulative maps as a function of the loading time in Fig. 5(j). The overall trend remains while the accuracies are improved at higher sampling rates, across the entire time horizon. At 1 GHz, the earlier states are not reconstructed as faithfully as the later ones due to the reduced order of information from the measurements. At the higher acquisition rates, the reconstruction accuracy of the intermediate states can be brought to a level similar to that of the final one. Because the wave propagation is a spatio-temporal phenomenon, if sensors could be placed arbitrarily in space, similar improvement should be possible by increasing the sampling density in time. Naturally, due to physical constraints, displacement sensors are generally placed on the surface of the sample, which impedes the potential improvement by increasing sensor density.

In this work, all sensors register their measurements simultaneously. In practice, however, they can operate asynchronously and at different rates, reducing the inter-dependency in the measurements and potentially further enhancing the reconstructions. While acquisition rates lower than 1 GHz have not been explored by the current study, primarily due to the computational demands of 3D-DDE simulations, the reconstruction approach holds promise for applications in lower frequency measurements such as AE. In the simulations presented here, dislocation motions are described in high spatial–temporal resolutions. In larger-scale problems with longer time horizons, a coarser-grain representation may suffice, reducing the need for fast measurements. Moreover, other physics-based or data-driven regularization techniques could further alleviate the ill-posedness of the reconstruction problem, making the reconstruction more feasible for lower acquisition rates.

In the current work, the location of sensor placement was based on maximizing the independence of the signals measured by each sensor. According to Eq. (1), sensors placed symmetrically around the dislocation slip location measure identical displacement signals, differing only in sign. In light of this fact, we removed sensors in an asymmetric way when reducing the number of sensors from 24 to 4, as shown in Fig. 4(b). Note that the current sensor placement was not specifically optimized for the single slip problem addressed in this work. While this placement should function similarly for different slip plane positions or even in cases with multiple slip planes, reconstruction accuracy may decrease if the acquisition rate and number of sensors remain unchanged, as the number of variables to be determined increases with multiple active slip planes. Alternative sensor configurations may offer improved performance, and investigating their impact is a promising direction for future research. If some sensors are placed significantly farther away from the dislocation slip plane than others, it will be important to consider that displacement magnitude decreases at a rate of $1/r^2$, where r is the distance from the dislocation slip position to the sensor. A large disparity will cause the current cost function (Eq. (4)) to over-emphasize the misfit in the stronger signals while neglecting the misfit in weaker ones. The accuracy of the reconstruction can be improved by optimally weighting the signals from different sensors in the definition of the cost function to reduce the uncertainty of the interpretation, or by optimizing the placement of the sensors, both being promising avenues for future study.

4.3. Effects of noise

The measurements adopted in the present reconstruction were sampled from a numerical simulation. As such, the only source of errors in the acquired measurements thus far has been the numerical discretization of the slip plane. This choice enables us to examine the performance of our algorithm absent uncertainties that are associated with experimental measurements, for example, to the sensor characteristics or environmental factors. It is nonetheless important to assess the robustness of the algorithm in presence of uncertainties. While there
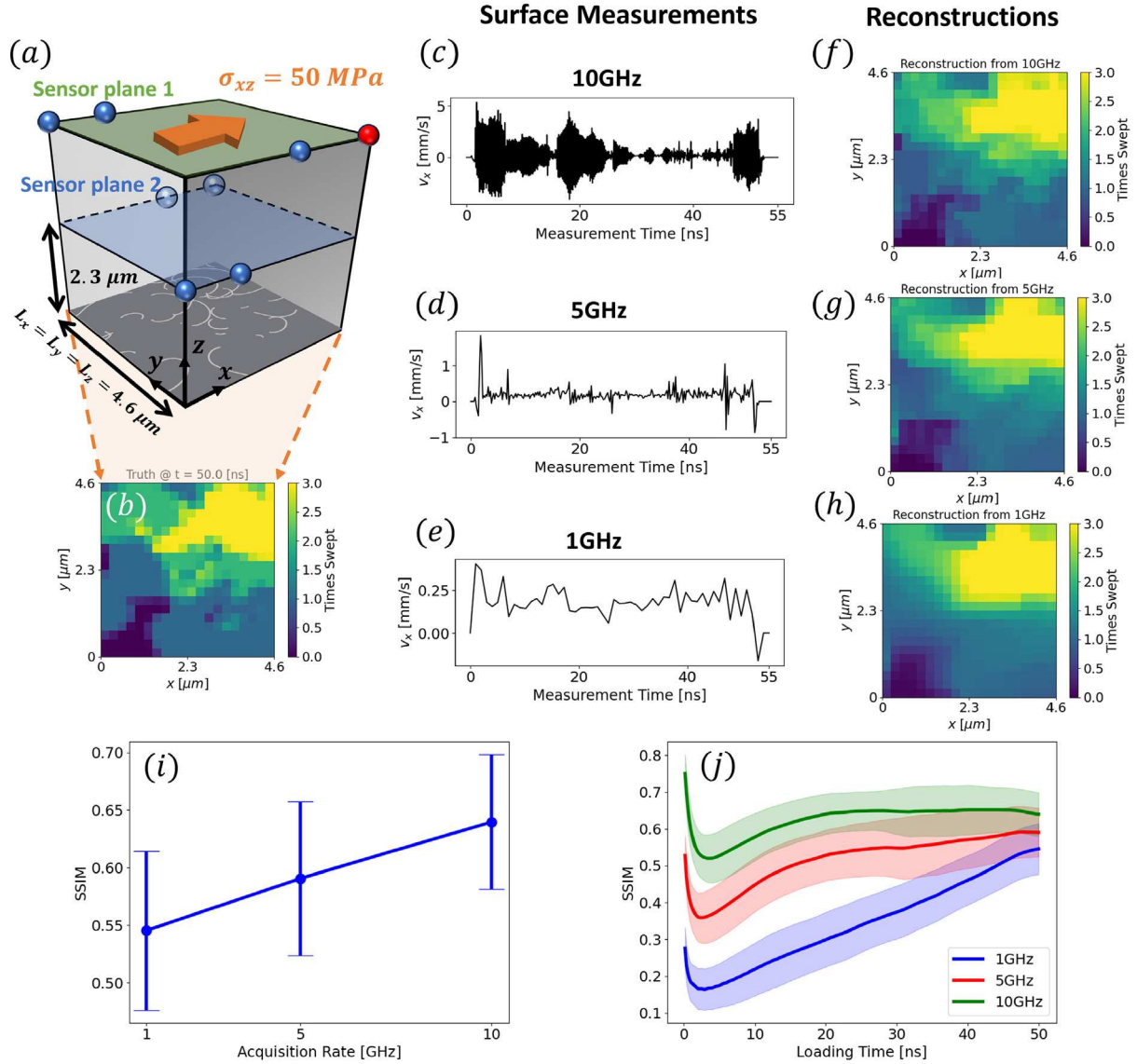
Fig. 5. The effect of acquisition rate on the reconstruction accuracy. (a) Schematic illustration of the configuration of DDE simulations and the placements of displacement sensors. (b) A representative cumulative swept-times map at the end of the simulation. The *x*-component of the surface velocity at the sensor marked red in (a) is shown for an acquisition rate of (c) 10; (d) 5; and (e) 1 GHz, respectively. The corresponding cumulative swept-times map for these three acquisition rates are shown in (f)–(h). The SSIM for the three cases are 0.70, 0.62 and 0.57, respectively. (i) Statistical plot of the reconstruction SSIM over 50 randomly initialized DDE simulations for each acquisition rate. The dots represent the mean SSIM, and the error bars indicate the standard deviation. (m) Statistical plot of the frame-by-frame reconstruction SSIM versus the simulation time. The curves are the mean SSIM at each time-step, and the bands indicate the standard deviation. (For interpretation of the references to color in this figure legend, the reader is referred to the web version of this article.)

are various noise filtering techniques available including principal component analysis, wavelet filtering and auto-encoders, noise-corrupted signals are used in the present reconstruction algorithm without any pre-processing. In this manner, we can direct the focus solely on the robustness of the algorithm.

The same fifty cases of DDE simulations described in Sections 4.1 and 4.2 and their corresponding elastodynamic measurements are used to examine the statistical influence of noise. Twenty four ($N_s = 24$) sensors operating at 1 GHz are used. The sensor configuration is the same as previously shown in Fig. 4(b). The noise level can be quantified by the signal-to-noise ratio (SNR) in decibel:

$$\text{SNR}_{\text{dB}} = 10 \log_{10}\left[\left(\frac{A_{\text{signal}}}{A_{\text{noise}}}\right)^2\right], \tag{16}$$

where A is the root mean square amplitude. In this discussion, additive Gaussian white noises with a SNR of 30 is introduced to corrupt the measurements. The signal corruption process is illustrated in Fig. 6(a)

for one of the sensors. Since the noise effectively reduces the confidence in the measurement data, the associated relative weighting in the cost function in Eq. (4) must be reduced. The order of magnitude for λ's are estimated empirically, using a grid search over an independent set of DDE simulations, thus, avoiding disclosing any information about the fifty cases that are used to assess the impact of the noise on our algorithm. The adopted weights in the cost function are $\lambda_t = 10^{-2}$ and $\lambda_x = \lambda_y = 10^{-4}$.

As an example, one of the underlying cumulative swept-times maps is displayed in Fig. 6(c), as well as the reconstruction from uncontaminated sensor data in Fig. 6(d). The prediction from the noisy signal is shown in Fig. 6(e). It is evident that the reconstruction is degraded, with edges blurred and mis-positioned due to the combined effects of noise and the strong TV minimization. However, useful information about the approximate locations and intensity is still preserved. For a statistical assessment, we compare the distribution of the reconstruction SSIM scores between the scenarios without and with signal noise in
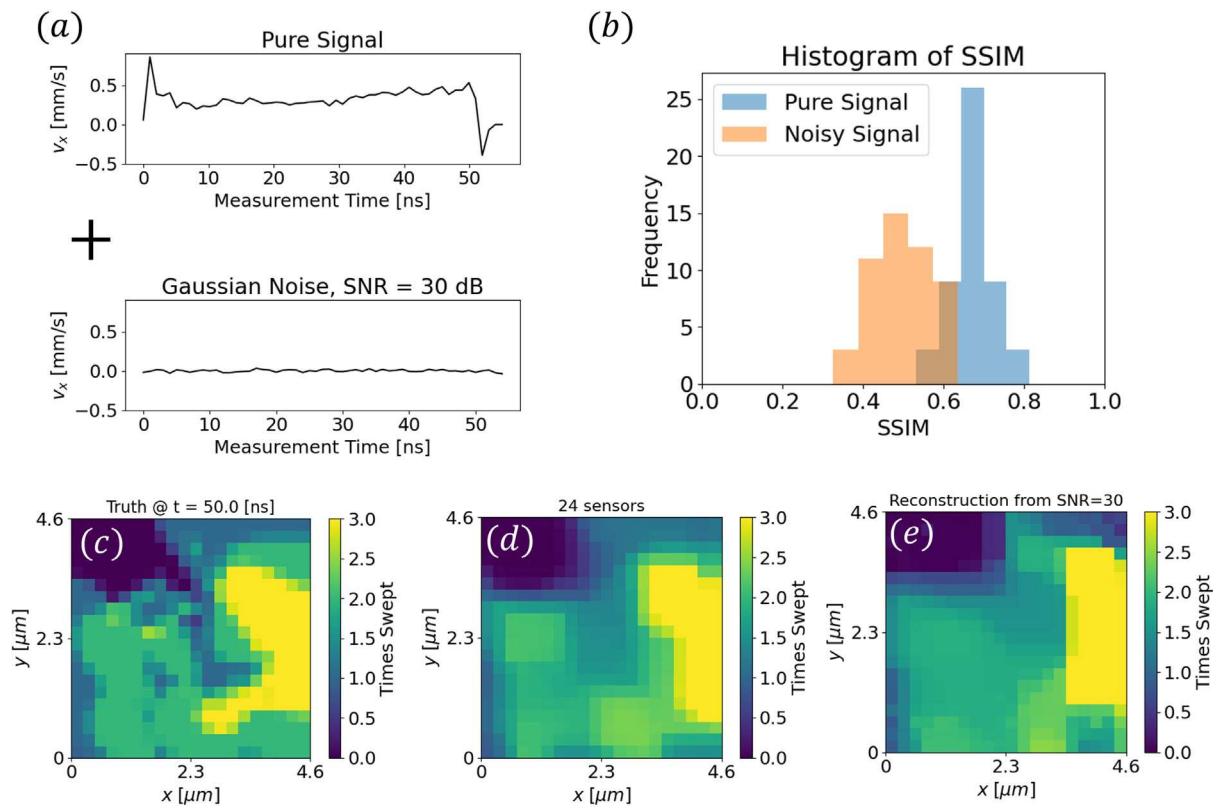
Fig. 6. The effect of noise in measurement on the reconstruction accuracy. (a) An example of a pure signal and the additive Gaussian white noise with SNR = 30 dB. (b) Distribution of reconstruction SSIM scores for 50 randomly initialized DDE simulations with pure and noisy measurements. (c) A representative cumulative swept-times map at the end of the simulation. (d) Reconstructed cumulative swept-times map using pure signals displaying an SSIM = 0.71. (e) Reconstructed cumulative swept-times map using noisy signals displaying an SSIM = 0.55.

Fig. 6(b). Though the SSIM score is reduced from 0.67 ± 0.05 to 0.50 ± 0.07, it is evident that the algorithm remains predictive, and can endure some extent of noise. In practice, pre-processing the noisy signals and leveraging prior knowledge about the source of noise would be adopted in order to minimize the impact of these uncertainties.

5. Conclusion

Dislocation slip is fundamental to crystal plasticity, but its localized and transient nature makes it challenging to fully resolve their evolution using conventional characterization techniques. In this work, we developed a reconstruction algorithm of dislocation slip evolution with high spatio-temporal resolution based on limited elastodynamic displacement measurements. This was achieved using the total-variation-regularized algorithm, which successfully compensates for the limited information in the measurements, as demonstrated using synthetic measurements from discrete dislocations elastodynamics simulations. We showed that increasing the number of sensors and their acquisition rate improves reconstruction accuracy, and the algorithm is robust to measurement noise.

Future research should focus on three key areas: (1) extending the algorithm to more complex deformation mechanisms involving multiple slip systems, (2) reducing the required number of sensors and acquisition rates to facilitate experimental adoption, and (3) examining additional factors such as boundary reflections.

Our data assimilation approach opens new avenues for characterizing and understanding the complex dynamics of crystal plasticity and designing advanced materials. With further development, it has the potential to revolutionize the study of intermittent plasticity and slip localization, as well as inspire new research at the intersection of experiments, simulations, and data-driven methods.

CRediT authorship contribution statement

Junjie Yang: Writing – review & editing, Writing – original draft, Visualization, Validation, Software, Project administration, Methodology, Investigation, Formal analysis, Data curation, Conceptualization. **Daniel Magagnosc:** Writing – review & editing, Validation, Supervision, Resources, Project administration, Methodology, Investigation, Funding acquisition. **Jaafar A. El-Awady:** Writing – review & editing, Writing – original draft, Visualization, Validation, Supervision, Software, Resources, Project administration, Methodology, Investigation, Funding acquisition, Formal analysis, Data curation, Conceptualization. **Tamer A. Zaki:** Writing – review & editing, Visualization, Validation, Supervision, Resources, Project administration, Methodology, Investigation, Funding acquisition, Formal analysis, Data curation, Conceptualization.

Declaration of competing interest

The authors declare that they have no known competing financial interests or personal relationships that could have appeared to influence the work reported in this paper.

Acknowledgments

References

[1] Dennis M Dimiduk, Chris Woodward, Richard LeSar, Michael D Uchic, Scale-free intermittent flow in crystal plasticity, Science 312 (5777) (2006) 1188–1190.

[2] Ferenc F Csikor, Christian Motz, Daniel Weygand, Michael Zaiser, Stefano Zapperi, Dislocation avalanches, strain bursts, and the problem of plastic forming at the micrometer scale, Science 318 (5848) (2007) 251–254.

[3] Jorge Alcalá, Jan Očenášek, Javier Varillas, Jaafar A. El-Awady, Jeffrey M Wheeler, Johann Michler, Statistics of dislocation avalanches in fcc and bcc metals: dislocation mechanisms and mean swept distances across microsample sizes and temperatures, Sci. Rep. 10 (1) (2020) 19024.

[4] Wei Li, Satish I Rao, Qingyuan Wang, Haidong Fan, Junjie Yang, Jaafar A El-Awady, Core structure and mobility of edge dislocations in face-centered-cubic chemically complex nicofe and nicofecu equiatomic solid-solution alloys, Materialia 9 (2020) 100628.

[5] Josh Kacher, IM Robertson, Quasi-four-dimensional analysis of dislocation inter-actions with grain boundaries in 304 stainless steel, Acta Mater. 60 (19) (2012) 6657–6672.

[6] JS Barnard, J Sharp, JR Tong, PA Midgley, High-resolution three-dimensional imaging of dislocations, Science 313 (5785) (2006) 319.

[7] Bo Yao, Danny J Edwards, Richard J Kurtz, Tem characterization of dislocation loops in irradiated bcc fe-based steels, J. Nucl. Mater. 434 (1–3) (2013) 402–410.

[8] Bassem Barkia, Jean-Philippe Couzinié, Sylvie Lartigue-Korinek, Ivan Guillot, Véronique Doquet, In situ tem observations of dislocation dynamics in α titanium: Effect of the oxygen content, Mater. Sci. Eng. A 703 (2017) 331–339.

[9] Josh Kacher, Ian M Robertson, In situ tem characterisation of dislocation interactions in α-titanium, Phil. Mag. 96 (14) (2016) 1437–1447.

[10] Ian Robinson, Ross Harder, Coherent x-ray diffraction imaging of strain at the nanoscale, Nat. Mater. 8 (4) (2009) 291–298.

[11] A Ulvestad, MJ Welland, W Cha, Y Liu, JW Kim, R Harder, E Maxey, JN Clark, MJ Highland, H You, et al., Three-dimensional imaging of dislocation dynamics during the hydriding phase transformation, Nat. Mater. 16 (5) (2017) 565–571.

[12] Mathew J Cherukara, Reeju Pokharel, Timothy S O'Leary, J Kevin Baldwin, Evan Maxey, Wonsuk Cha, Jorg Maser, Ross J Harder, Saryu J Fensin, Richard L Sandberg, Three-dimensional x-ray diffraction imaging of dislocations in polycrystalline metals under tensile loading, Nat. Commun. 9 (1) (2018) 3776.

[13] JN Clark, L Beitra, G Xiong, A Higginbotham, DM Fritz, HT Lemke, D Zhu, M Chollet, GJ Williams, Marc Messerschmidt, et al., Ultrafast three-dimensional imaging of lattice dynamics in individual gold nanocrystals, Science 341 (6141) (2013) 56–59.

[14] Jerome Weiss, Jean-Robert Grasso, Acoustic emission in single crystals of ice, J. Phys. Chem. B 101 (32) (1997) 6113–6117.

[15] LM Barker, RE Hollenbach, Laser interferometer for measuring high velocities of any reflecting surface, J. Appl. Phys. 43 (11) (1972) 4669–4675.

[16] Junjie Yang, Ali Rida, Yejun Gu, Daniel Magagnosc, Tamer A Zaki, Jaafar A El-Awady, The three-dimensional elastodynamic solution for dislocation plasticity and its implementation in discrete dislocation dynamics simulations, Acta Mater. 253 (2023) 118945.

[17] Yinan Cui, Giacomo Po, Yves-Patrick Pellegrini, Markus Lazar, Nasr Ghoniem, Computational 3-dimensional dislocation elastodynamics, J. Mech. Phys. Solids 126 (2019) 20–51.

[18] T Mura, Continuous distribution of moving dislocations, Phil. Mag. 8 (89) (1963) 843–857.

[19] Gabor T Herman, Fundamentals of Computerized Tomography: Image Reconstruction from Projections, Springer Science & Business Media, 2009.

[20] Ge Wang, Yi Zhang, Xiaojing Ye, Xuanqin Mou, Machine Learning for Tomographic Imaging, IOP Publishing, 2019.

[21] Rafael C Gonzalez, Richard E Woods, Digital Image Processing, Prentice Hall, upper saddle river. J., 2002.

[22] Alejandro Ribes, Francis Schmitt, Linear inverse problems in imaging, IEEE Signal Process. Mag. 25 (4) (2008) 84–99.

[23] Vincent Mons, Qi Wang, Tamer A Zaki, Kriging-enhanced ensemble variational data assimilation for scalar-source identification in turbulent environments, J. Comput. Phys. 398 (2019) 108856.

[24] Tamer A. Zaki, Turbulence from an observer perspective, Annu. Rev. Fluid Mech. (2024).

[25] Tamer A. Zaki, Mengze Wang, From limited observations to the state of turbulence: Fundamental difficulties of flow reconstruction, Phys. Rev. Fluids 6 (10) (2021) 100501.

[26] V. Mons, Y. Du, T.A. Zaki, Ensemble-variational assimilation of statistical data in large-eddy simulation, Phys. Rev. Fluids 6 (2021) 104607.

[27] D.A. Buchta, T.A. Zaki, Observation-infused simulations of high-speed boundary-layer transition, J. Fluid Mech. 916 (A44) (2021).

[28] D.A. Buchta, Stuart J. Laurence, T.A. Zaki, Assimilation of wall-pressure measurements in high-speed flow over a cone, J. Fluid Mech. 947 (R2) (2022).

[29] Athanasios Arsenlis, Wei Cai, Meijie Tang, Moono Rhee, Tomas Oppelstrup, Gregg Hommes, Tom G Pierce, Vasily V Bulatov, Enabling strain hardening simulations with dislocation dynamics, Modelling Simul. Mater. Sci. Eng. 15 (6) (2007) 553.

[30] Ahmed M Hussein, Satish I Rao, Michael D Uchic, Dennis M Dimiduk, Jaafar A El-Awady, Microstructurally based cross-slip mechanisms and their effects on dislocation microstructure evolution in fcc crystals, Acta Mater. 85 (2015) 180–190.

[31] Benoit Devincre, Ladislas P Kubin, Mesoscopic simulations of dislocations and plasticity, Mater. Sci. Eng. A 234 (1997) 8–14.

[32] N Ghoniem, M, S-H. Tong, LZ Sun, Parametric dislocation dynamics: a thermodynamics-based approach to investigations of mesoscopic plastic deformation, Phys. Rev. B 61 (2) (2000) 913.

[33] Daniel Weygand, LH Friedman, E Van der Giessen, A Needleman, Aspects of boundary-value problem solutions with three-dimensional dislocation dynamics, Modelling Simul. Mater. Sci. Eng. 10 (4) (2002) 437.

[34] Marc Fivel, Christophe Depres, An easy implementation of displacement calcu-lations in 3d discrete dislocation dynamics codes, Phil. Mag. 94 (28) (2014) 3206–3214.

[35] Wei Cai, Athanasios Arsenlis, Christopher R Weinberger, Vasily V Bulatov, A non-singular continuum theory of dislocations, J. Mech. Phys. Solids 54 (3) (2006) 561–587.

[36] Leonid I Rudin, Stanley Osher, Emad Fatemi, Nonlinear total variation based noise removal algorithms, Physica D 60 (1–4) (1992) 259–268.

[37] Emil Y Sidky, Chien-Min Kao, Xiaochuan Pan, Accurate image reconstruction from few-views and limited-angle data in divergent-beam ct, J. X-Ray Sci. Technol. 14 (2) (2006) 119–139.

[38] Yilun Wang, Junfeng Yang, Wotao Yin, Yin Zhang, A new alternating minimiza-tion algorithm for total variation image reconstruction, SIAM J. Imaging Sci. 1 (3) (2008) 248–272.

[39] Jorge Nocedal, Updating quasi-newton matrices with limited storage, Math. Comput. 35 (151) (1980) 773–782.

[40] Jorge Nocedal, Stephen J Wright, Numerical Optimization, Springer, 1999.

[41] Zhou Wang, Alan C Bovik, Mean squared error: Love it or leave it? a new look at signal fidelity measures, IEEE Signal Process. Mag. 26 (1) (2009) 98–117.

[42] Zhou Wang, Alan C Bovik, Hamid R Sheikh, Eero P Simoncelli, Image quality assessment: from error visibility to structural similarity, IEEE Trans. Image Process. 13 (4) (2004) 600–612.